Intelligent and Sustainable Manufacturing

SciEPublish

Article

Microstructure, Phase Stability, and Mechanical Performance of a Laser Directed Energy Deposition Ti-6Al-4V

Ajay Panthri [1,*], Arun Kumar Rai [1,2], Pooja Patidar [1,2], Christ Prakash Paul [1,2]

[1] Engineering Design and Manufacturing Division, Raja Ramanna Centre for Advanced Technology, Indore 452013, India; akrai@rrcat.gov.in (A.K.R.); poojap@rrcat.gov.in (P.P.); paulcp@rrcat.gov.in (C.P.P.)

[2] Homi Bhabha National Institute, Anushakti Nagar, Mumbai 400094, India

* Corresponding author. E-mail: pajay@rrcat.gov.in (A.P.)

Received: 15 September 2026; Revised: 12 October 2026; Accepted: 19 November 2026; Available online: 26 November 2026

ABSTRACT: This study investigates the process-microstructure-phase-property correlation of Ti-6Al-4V alloy fabricated via Laser Directed Energy Deposition (LDED). A full-factorial 27 single-tracks experimental matrix was initially conducted by varying laser power (700–900 W), scanning speed (500–700 mm/min), and powder feed rate (2.8–4.0 g/min) to determine an optimized deposition condition based on geometrical integrity and cross-sectional morphology. The optimal parameters were identified as 900 W laser power, 600 mm/min scanning speed, and 3.4 g/min powder feed rate. Bulk components fabricated under these conditions achieved a high density of 99.54% (porosity < 0.5%), as confirmed by X-ray micro-computed tomography (micro-CT) and Archimedes' principle. Microstructural characterisation via optical microscopy, Field Emission Scanning Electron Microscopy (FESEM), Electron Backscatter Diffraction (EBSD), and Synchrotron X-ray Diffraction (XRD) revealed that the deposit features highly elongated prior-β grains oriented along the build direction due to directional solidification and epitaxial growth. The hierarchical intragranular structure is predominantly composed of fine acicular/lenticular α' martensite variants (93.5% α/α' phase fraction) containing crystallographic nano-twins to accommodate rapid non-equilibrium transformation strains, alongside a 6.5% fraction of retained β phase in globular and lamellar morphologies. Mechanical evaluation revealed a progressive step-up in microhardness across the boundary zones, rising from 174–176 $HV^{0.1}$ in the unaffected substrate to 187–241 $HV^{0.1}$ in the heat-affected zone (HAZ), and peaking at 377–434 $HV^{0.1}$ within the deposited region. The spatial fluctuations in the deposit's microhardness profile serve as a mechanical footprint of *in-situ* tempering and partial α' martensite decomposition induced by layer-by-layer thermal cycling. Room-temperature tensile testing demonstrated excellent, robust mechanical properties across all primary axes, with ultimate tensile strength (UTS) values ranging from 980 to 1000 MPa and total elongation to failure ranging from 18% to 18.5%. While the ultimate strength and fracture strain values remain highly isotropic, distinct anisotropic behaviour was observed during yielding and early strain-hardening regimes when specimens were loaded parallel to the long axis of the columnar prior-β boundaries along the build direction.

Keywords: Ti-6Al-4V; Laser directed energy deposition (LDED); Process parameter optimization; Synchrotron XRD; Martensitic transformation; Nano-twins; Microhardness heterogeneity; Tensile anisotropy

© 2026 The authors. This is an open access article under the Creative Commons Attribution 4.0 International License (https://creativecommons.org/licenses/by/4.0/).

1. Introduction

Ti-6Al-4V is an $\alpha + \beta$ titanium alloy widely employed in aerospace, biomedical, and other high-performance applications owing to its high specific strength, low density, excellent corrosion resistance, and favorable mechanical properties. However, the manufacture of complex Ti-6Al-4V components by conventional processing routes is often associated with substantial material wastage and limitations in geometric complexity. Laser directed energy deposition (LDED) has emerged as a promising additive manufacturing technique for near-net-shape fabrication and repair of titanium components. In LDED, metallic powder is delivered into a laser-generated melt pool, where it is melted and subsequently solidified to form successive tracks and layers. The characteristics of the deposited material are strongly influenced by the coupled effects of laser power, scanning speed, and powder feed rate, which determine the energy input, material deposition rate, melt-pool geometry, and solidification conditions [1–4]. Consequently, selecting appropriate process parameters is essential to achieve continuous deposition with adequate geometrical and metallurgical integrity.

The microstructure developed during LDED of Ti-6Al-4V is primarily governed by its highly transient thermal history. Rapid melting and solidification are followed by repeated thermal exposure as successive tracks and layers are deposited, resulting in spatially varying temperature gradients and cooling conditions. The steep thermal gradients promote directional solidification and epitaxial growth of prior-β grains, leading commonly to elongated columnar grains preferentially oriented along the build direction [5–7]. Kelly and Kampe [6] reported the development of columnar prior-β grains and variations in α-lath morphology in multilayer laser deposited Ti-6Al-4V, demonstrating the significant influence of the layer-wise thermal cycle on microstructural evolution. Similarly, Tan et al. [8] observed elongated epitaxial prior-β grains in LDED built Ti-6Al-4V and attributed their development to directional heat flow during deposition. The resulting prior-β grain morphology therefore reflects the local solidification conditions and provides an important microstructural record of the thermal history imposed during LDED.

The subsequent transformation of the β phase during cooling further determines the phase constitution and morphology of the deposited alloy. Depending on the cooling rate and thermal exposure, the β phase can undergo diffusional transformation to $\alpha + \beta$ constituents or diffusionless transformation to metastable α' martensite under sufficiently rapid cooling conditions [6–9]. Accordingly, LDED built Ti-6Al-4V can exhibit a hierarchical microstructure consisting of prior-β grains containing fine acicular α/α' transformation products together with retained β. The repeated reheating associated with multilayer deposition can further modify these transformation products and produce spatial variations in their morphology and distribution [6,8]. Such microstructural evolution has a direct influence on the mechanical response of the deposited material. In particular, fine α' dominated structures generally exhibit higher microhardness than relatively coarse $\alpha + \beta$ microstructures because of supersaturation, lattice strain, high defect density, and the increased density of interfaces that impede dislocation motion [9–11]. Thus, establishing the relationship between the thermal history, phase transformation, and the resulting microstructure is essential for understanding the mechanical behavior of LDED built Ti-6Al-4V.

In addition to thermal history, the processing environment can influence the phase stability and properties of Ti-6Al-4V because of its high affinity for interstitial elements at elevated temperatures. Inadequate shielding during laser processing can promote oxygen and nitrogen uptake, which may alter phase stability, microstructure, microhardness, and defect formation [12]. Studies comparing different melt-pool protection conditions have demonstrated that the extent of environmental interaction can significantly affect the microstructural and mechanical characteristics of laser deposited Ti-6Al-4V [12]. However, the effects associated with the processing environment are coupled with those arising from laser energy input, cooling conditions, and repeated thermal cycling. Consequently, interpreting microstructural and

microhardness variations requires considering the combined thermal and processing history rather than attributing observed changes to a single factor [13,14].

Despite extensive investigations into the processing and microstructural characteristics of additively manufactured Ti-6Al-4V, a comprehensive understanding of the relationship between process-parameter selection, local thermal history, prior-β grain morphology, phase constitution, elemental partitioning, and microhardness across the substrate–heat-affected zone (HAZ)–deposit region remains important [15–18]. In particular, single-track geometrical characteristics alone may not adequately represent deposition quality, since tracks with comparable dimensions or aspect ratios (W/H) can exhibit differences in continuity, fusion characteristics, porosity, and cracking. Furthermore, although columnar prior-β grains and α' martensitic structures in LDED built Ti-6Al-4V have been extensively reported, their spatial evolution from the substrate and HAZ into the deposited region, together with the corresponding phase and microhardness variations, warrants further investigation under specific processing conditions [19–22]. A combined microstructural and crystallographic assessment is also desirable because α and α' possess closely related hexagonal crystal structures and may not always be distinguished unambiguously using morphology or conventional diffraction alone [23–25].

Therefore, the present study investigates the microstructural and phase evolution of Ti-6Al-4V fabricated by LDED and its correlation with microhardness. A systematic full-factorial single-track investigation was initially conducted by varying laser power, scanning speed, and powder feed rate to identify a suitable processing condition based on both track geometry and cross-sectional morphological integrity. The selected condition was subsequently employed for the bulk deposition. The substrate, HAZ, and deposited regions were systematically characterized using optical microscopy, field-emission scanning electron microscopy, electron backscattered diffraction (EBSD), energy-dispersive spectroscopy, synchrotron X-ray diffraction, Vickers microhardness measurements, and tensile test. Particular attention was given to the evolution of prior-β grain morphology, α/α' transformation products, retained β, and elemental partitioning, and their relationship with the spatial microhardness distribution. This integrated approach provides a process–microstructure–phase–property correlation for LDED built Ti-6Al-4V and clarifies the role of the deposition thermal history in governing the microstructural and mechanical heterogeneity of the fabricated component.

2. Materials and Methods

2.1. Laser Directed Energy Deposition

Gas-atomized Ti-6Al-4V powder (manufacturer: MatrixNano, Noida, India) was used as the feedstock for laser directed energy deposition (LDED). The powder particles were predominantly spherical, with particle sizes ranging from 45 to 105 µm. The SEM micrograph of Ti-6Al-4V powder particles and their particle size distribution are provided in Figure 1a,b. The majority of particles have a size in the range of 55–65 µm. A sandblasted cylindrical commercially pure titanium (CP-Ti) substrate, measuring 50 mm in diameter and 8 mm in thickness, was selected to ensure metallurgical compatibility with the deposited alloy. The composition of both the substrate and Ti-6Al-4V was ensured using a Elemental composition was determined using a handheld X-ray fluorescence (XRF) spectrometer (S1 TITAN 500, Bruker Nano Analytics, Kennewick**,** WA, USA). The LDED system consisted of a five-axis CNC workstation, a continuous-wave (CW) 2 kW ytterbium-doped fiber laser operating at a wavelength of 1070 nm, and two powder hoppers [13]. A schematic of the LDED system used in the present study is shown in Figure 2. During deposition, the substrate was mounted on the CNC workstation, and Ti-6Al-4V powder was delivered to the deposition nozzle using argon as a carrier gas. In addition to the carrier gas, protective argon gas was also streamed along the laser beam on the substrate to protect the melt-pool from oxidation. The laser beam generated a melt pool on the substrate, into which the powder particles were injected, melted,

and subsequently solidified to form the deposited material. A bulk Ti-6Al-4V deposit measuring approximately 20 × 10 × 10 mm^3 was fabricated using a laser power of 900 W, a scanning speed of 600 mm/min, and a powder feed rate of 3.4 g/min. These parameters were selected based on preliminary single-track deposition trials and the resulting geometric and morphological integrity across the 27 single tracks. For bulk geometry, a layer thickness of 0.6 mm and a track overlap ratio of 50% were utilized. The deposition followed a bidirectional scanning strategy, with a deposition path that was rotated by 90° between successive layers to minimize residual stress and ensure uniform thermal distribution.

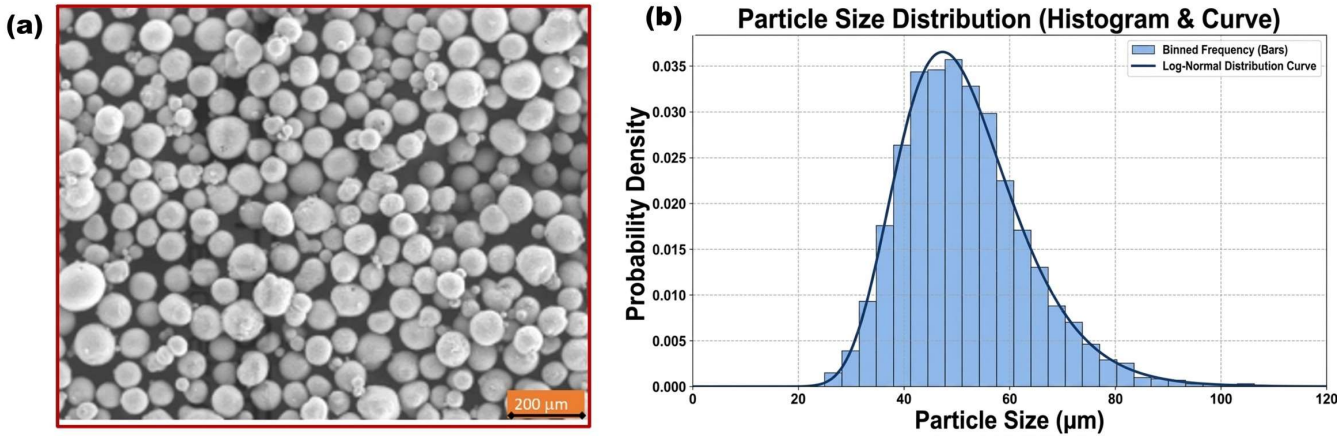

Figure 1. (**a**) SEM micrograph of Ti-6Al-4V powder particles and (**b**) Powder particle size distribution.

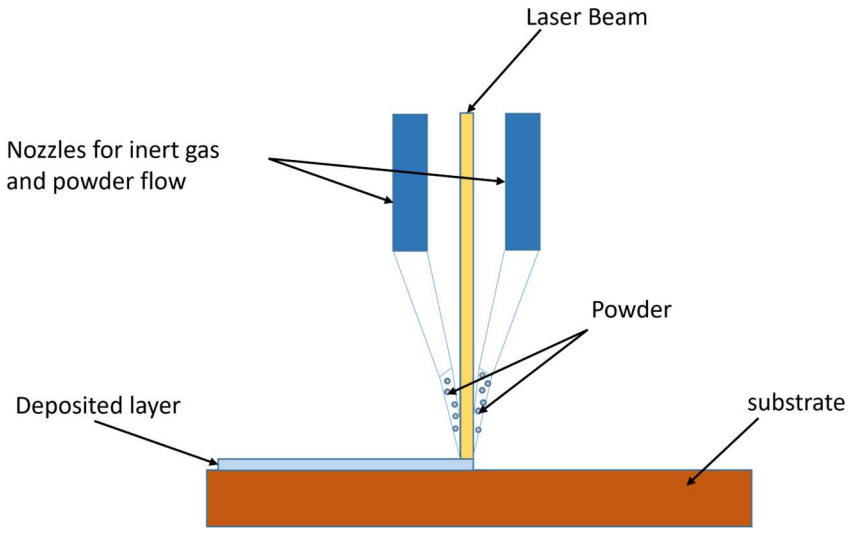

Figure 2. Schematic of LDED process used in the present study.

2.2. Defect Characterisation Using X-ray Micro-Computed Tomography

The internal integrity of the LDED-fabricated Ti-6Al-4V deposit was evaluated using X-ray micro-computed tomography (micro-CT) with a GE Phoenix v|tome|x C450 system. The scans were performed at an accelerating voltage of 250 kV and a tube current of 3.2 mA, with a nominal spatial resolution of approximately 20 µm. The reconstructed volumetric data were analyzed using VGSTUDIO MAX software with version: 2026.2 and the vgi_pore_analysis workflow. Defect segmentation was performed using the ISO-50 surface determination method and a VGDefX setting of 0.90, with an eight-voxel cutoff applied to exclude features below the selected minimum voxel threshold. The reconstructed volume was examined for detectable internal defects, including pores, lack-of-fusion (LOF) regions, and cracks. The three-dimensional dataset enabled assessment of the spatial distribution and morphology of detectable defects within the scanned

volume. The effective detectability of individual defects depended on their dimensions, orientation, contrast relative to the surrounding material, and the imaging and segmentation conditions. Accordingly, the micro-CT results were interpreted in terms of defects detectable under the selected scanning and analysis conditions.

2.3. Microstructural and Structural Characterisation

Following deposition and micro-CT examination, specimens were extracted from the deposited block using electrical discharge machining (EDM). A specimen measuring approximately 10 × 5 × 3 mm^3 was sectioned vertically to expose the cross-section of the deposit, substrate, and interface for microstructural characterisation. The specimen was mounted in epoxy resin using a resin-to-hardener ratio of 2:1. After curing, the specimen was ground using abrasive papers ranging from P150 to P1200 grit and subsequently polished with alumina gel to obtain a surface finish of approximately 1 µm. The polished surface was etched with Kroll's reagent, consisting of 92 mL of distilled water, 6 mL of nitric acid (HNO_3), and 2 mL of hydrofluoric acid (HF) for approximately 30–50 s. The prepared and etched specimens were examined using a Leica DM 2700 M optical microscope to investigate the overall microstructure and its variation across the substrate, heat-affected zone (HAZ), and deposited region. Detailed microstructural characterisation was performed using a Zeiss field-emission scanning electron microscope (FESEM). Where applicable, energy-dispersive X-ray spectroscopy (EDS) was used to investigate elemental distribution and partitioning within the microstructure.

Electron backscatter diffraction (EBSD) analysis was performed to characterize crystallographic orientations, grain structures, and grain-boundary characteristics. The EBSD measurements were conducted at an accelerating voltage of 20 kV, a probe current of 5 nA, and a specimen tilt angle of 72°, using a step size of 0.1 µm to resolve crystallographic features at the scale of the microstructural constituents. The acquired EBSD patterns were subsequently processed to obtain crystallographic orientation maps and grain-boundary information from the analysed regions. Synchrotron X-ray diffraction measurements were performed at beamline BL-02 of the INDUS-2 synchrotron radiation source facility at RRCAT. An X-ray energy of 17 keV was used to examine the phase constitution of the deposited Ti-6Al-4V. The diffraction pattern was analysed by comparing the observed reflections with the characteristic peaks of the α/α', β, and possible α'' phases. Phase assignments were interpreted cautiously where diffraction peaks overlapped.

2.4. Mechanical Property Characterisation

Vicker's microhardness measurements were performed to evaluate local microhardness variations across the substrate, HAZ, and deposited region. Measurements were conducted using a test load of 0.1 kgf ($HV^{0.1}$) and a dwell time of 10 s. Indentations were placed in the relevant regions of the cross-section to compare the microhardness of the substrate, thermally affected region, and deposited material. For each location, a minimum of three microhardness measurements were acquired, and their average is presented along with the associated error. Between consecutive indentations, a minimum gap of 0.2 mm is kept to avoid the effect of the plastically deformed region. The measured microhardness values were correlated with the observed microstructural characteristics and phase constitution to examine the relationship between local structural features and resistance to indentation. Tensile specimens were machined from the LDED built Ti-6Al-4V using EDM. The tensile specimen had a gauge length of 12 mm, a gauge width of 4 mm, a thickness of 2 mm, and a fillet radius of 6 mm. The specimens were extracted from the deposited material, and their dimensions were selected to accommodate the available deposit geometry. Tensile testing was performed to evaluate the mechanical response of the deposited material. The recorded load and deformation data were used to determine tensile properties, including ultimate tensile strength and elongation, as supported by the measurements. The tensile results were interpreted in conjunction with the

micro-CT defect assessment, microstructural characterisation, phase analysis, and microhardness measurements to examine the relationship between structural features and mechanical performance.

3. Results and Discussion

3.1. Experimental and Numerical Process Parameters Optimization for Defect-Free Deposition

A systematic single-track investigation was conducted to identify a suitable processing condition for laser directed energy deposition (LDED) of Ti-6Al-4V. A full-factorial experimental design comprising 27 single-tracks experiments was performed by varying laser power, scanning speed, and powder feed rate over the ranges of 700–900 W, 500–700 mm/min, and 2.8–4.0 g/min, respectively. The complete experimental matrix, calculated linear energy density (LED), and corresponding geometrical characteristics of the deposited tracks are presented in Table 1.

Table 1. Effect of Process Parameters on Track Width, Height and Aspect ratio.

S. NO.	Powder Feed Rate (g/min)	Power (W)	Scanning Speed (mm/min)	Linear Energy Density (J/mm)	Track W (mm)	Track Height (mm)	Aspect Ratio (W/H)
1	2.8	700	500	84	2.117	0.459	4.61
2	2.8	700	600	70	2.073	0.222	9.33
3	2.8	700	700	60	2.191	0.324	6.76
4	2.8	800	500	96	2.359	0.359	6.57
5	2.8	800	600	80	2.327	0.254	9.16
6	2.8	800	700	69	2.225	0.257	8.65
7	2.8	900	500	108	2.206	0.394	5.59
8	2.8	900	600	90	2.534	0.313	8.09
9	2.8	900	700	77	2.401	0.281	8.54
10	3.4	700	500	84	2.119	0.348	6.08
11	3.4	700	600	70	2.212	0.345	6.41
12	3.4	700	700	60	2.01	0.282	7.12
13	3.4	800	500	96	2.307	0.427	5.40
14	3.4	800	600	80	2.267	0.479	4.73
15	3.4	800	700	69	2.212	0.345	6.41
16	3.4	900	500	108	2.604	0.47	5.54
17	3.4	900	600	90	2.502	0.332	7.54
18	3.4	900	700	77	2.5	0.347	7.20
19	4	700	500	84	1.947	0.343	5.67
20	4	700	600	70	2.041	0.374	5.45
21	4	700	700	60	2.071	0.437	4.73
22	4	800	500	96	2.302	0.54	4.26
23	4	800	600	80	2.225	0.383	5.80
24	4	800	700	69	2.041	0.374	5.45
25	4	900	500	108	2.59	0.427	6.06
26	4	900	600	90	2.479	0.349	7.10
27	4	900	700	77	2.327	0.447	5.20

The linear energy density was calculated using the following equation:

$$\text{LED} = \frac{60P}{V} \tag{1}$$

where P is the laser power in W and scanning speed V is in mm/min.

The calculated linear energy density (LED) values ranged from 60 to 108 J/mm. While LED (the nominal incident laser energy supplied per unit travel distance) and the width-to-height aspect ratio ($\frac{W}{H}$) are

useful for comparing processing conditions, neither serves as a standalone indicator of deposition quality. Consequently, track geometry was evaluated alongside cross-sectional morphology, continuity, and visible defects. Figure 3 presents nine representative optical macrographs from the 27 single-tracks experiment, illustrating the combinations of three laser powers (700, 800, and 900 W), three scanning speeds (500, 600, and 700 mm/min), and three powder feed rates (2.8, 3.4, and 4.0 g/min). Table 1 demonstrates substantial variations in track geometry across the processing window, proving that dimensions depend on the non-linear, coupled effects of laser power, scanning speed, and powder feed rate. Specifically, at a fixed powder feed rate of 2.8 g/min, increasing the scanning speed from 500 to 700 mm/min decreased the LED across all power levels. At 700 W, the LED decreased from 84 to 60 J/mm, and the track width ranged from 1.947 to 2.212 mm, while the height ranged from 0.222 to 0.459 mm. At 800 W, the track width ranged from 2.041 to 2.359 mm and the height ranged from 0.254 to 0.540 mm. At 900 W, the width ranged from 2.206 to 2.604 mm and the height from 0.281 to 0.470 mm. The geometrical response to these changing parameters is not strictly linear. For example, at 900 W and 3.4 g/min, increasing the scanning speed from 500 to 600 mm/min reduced the LED from 108 to 90 J/mm. This caused a considerable drop in track height from 0.470 to 0.332 mm but only a modest decrease in width from 2.604 to 2.502 mm, effectively increasing the $\frac{W}{H}$ ratio from 5.54 to 7.54. Further increasing the scanning speed to 700 mm/min produced minimal width changes but slightly increased the height. Furthermore, the influence of the powder feed rate demonstrates that even at a constant LED, track geometry fluctuates based on material supply [13,19,21]. At 900 W and 600 mm/min, where the LED remains constant at 90 J/mm, increasing the powder feed rate from 2.8 to 4.0 g/min increased the track height from 0.313 to 0.349 mm and decreased both the track width (from 2.534 to 2.479 mm) and the $\frac{W}{H}$ ratio (from 8.09 to 7.10). These trends demonstrate that higher laser power promotes lateral spreading, faster scanning speed reduces interaction time, and higher powder feed rate supplies more material to the melt pool while altering the energy distributed per unit mass. Because neither a higher LED nor a higher.

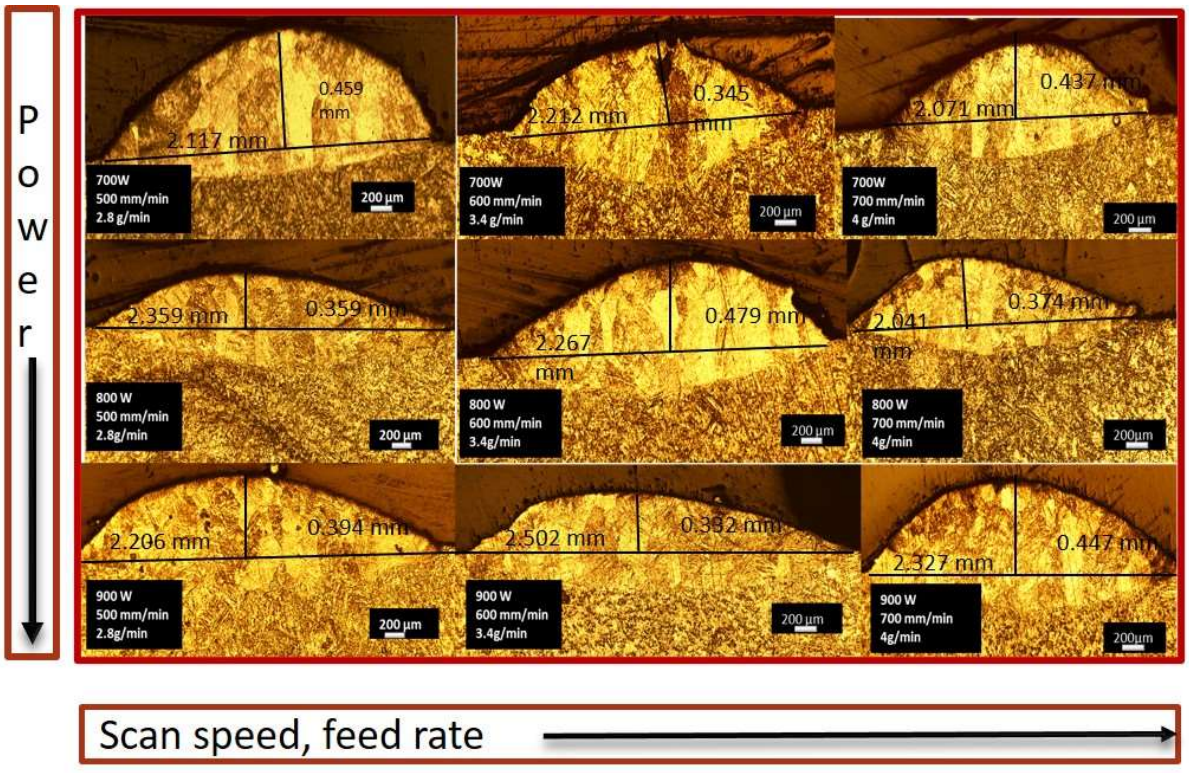

Figure 3. Optical macrographs of the single tracks of LDED built Ti-6Al-4V alloy obtained at selected process parameters where minimum porosity and crack formation are observed.

$\frac{W}{H}$ guarantees superior deposition, parameters must be selected holistically. Therefore, an ANOVA (Analysis of Variance)-based statistical significance and global response surface optimization become essential, and, in this context, ANOVA-based analysis was performed to establish a fully validated process window.

To quantify the relationships between the processing parameters and the resulting track geometry, a Response Surface Methodology (RSM) analysis and Pearson correlation assessment were performed for the track aspect ratio ($\frac{W}{H}$), and corresponding results are presented in Figure 4a–d. The Pearson correlation matrix reveals that the powder flow rate possesses the strongest individual correlation with the aspect ratio (W/H) ($r = -0.54$), followed by weak positive correlations with scanning speed ($r = 0.25$) and laser power ($r = 0.22$). Notably, the linear energy density (LED) exhibits a negligible correlation with the aspect ratio (W/H) ($r = -0.10$), which statistically reinforces the observation that LED alone cannot reliably predict deposition geometry [23]. The RSM ANOVA results indicate that the interaction between laser power and scanning speed (P:V) exerts the strongest relative influence on the aspect ratio (W/H), yielding the highest F-value among the evaluated terms. However, none of the individual parameters, squared terms, or two-way interactions crossed the statistical significance threshold of $p < 0.05$. Consequently, the resulting RSM predictive model yields a moderate fit, with a coefficient of determination (R^2) of 0.540 and a root mean square error (RMSE) of 0.911. These statistical findings suggest that, although parameter interactions, particularly those between laser power and scanning speed, influence geometric variations, the inherent variability of single-track LDED processes limits the accuracy of statistical predictions of the width-to-height aspect ratio (W/H) based solely on these three primary processing parameters [14]. This further justifies the necessity of selecting optimal parameters through a combined qualitative and quantitative assessment of morphology and geometry, rather than relying strictly on surface-response optimization.

Based on this combined assessment of regular cross-sectional morphology, track geometry, and minimum porosity, the condition of 900 W laser power, 600 mm/min scanning speed, and 3.4 g/min powder feed rate was selected as the most favourable starting point for bulk Ti-6Al-4V deposition. This combination yields an LED of 90 J/mm, a relatively wide track of 2.502 mm, a low height of 0.332 mm, and an aspect ratio (W/H) of 7.54. The optimised parameter conditions are noted in Table 2. It should be noted that while the 27 single track experiments constitute a full-factorial arrangement, the factor-level averages presented are descriptive. After bulk deposition, 3D porosity and defect characterization were performed on bulk-deposited Ti-6Al-4V. To complement the two-dimensional metallographic observations, X-ray micro-computed tomography (micro-CT) was performed to examine the internal structure of the bulk deposit using the selected condition of 900 W, 600 mm/min, and 3.4 g/min. Figure 5a–c shows representative two-dimensional cross-sectional slices from the top, middle, and bottom regions of the LDED built Ti-6Al-4V, while Figure 5d presents the corresponding three-dimensional micro-CT reconstruction. A small number of isolated pores can be observed within the examined volume. Although approximately spherical and irregular pore morphologies may be associated with gas entrapment and incomplete melting, respectively, their origins cannot be conclusively determined from morphology alone [13]. The three-dimensional reconstruction does not reveal extensive interconnected pore networks or large internal discontinuities within the scanned volume, indicating comparatively good internal structural continuity. The porosity estimated from the micro-CT examination was less than 0.5%. This observation is consistent with the Archimedes density measurements, which yielded a relative density of 99.54% of the theoretical density. The reported value represents the average of at least three independent measurements. Although further quantitative analysis would be required to establish a detailed pore-size distribution and validate pore classification, the micro-CT and density measurements jointly indicate a low level of internal porosity in the selected deposit. These findings, together with the single-track geometry assessment, support the selection of the investigated processing condition for subsequent microstructural and mechanical characterisation.

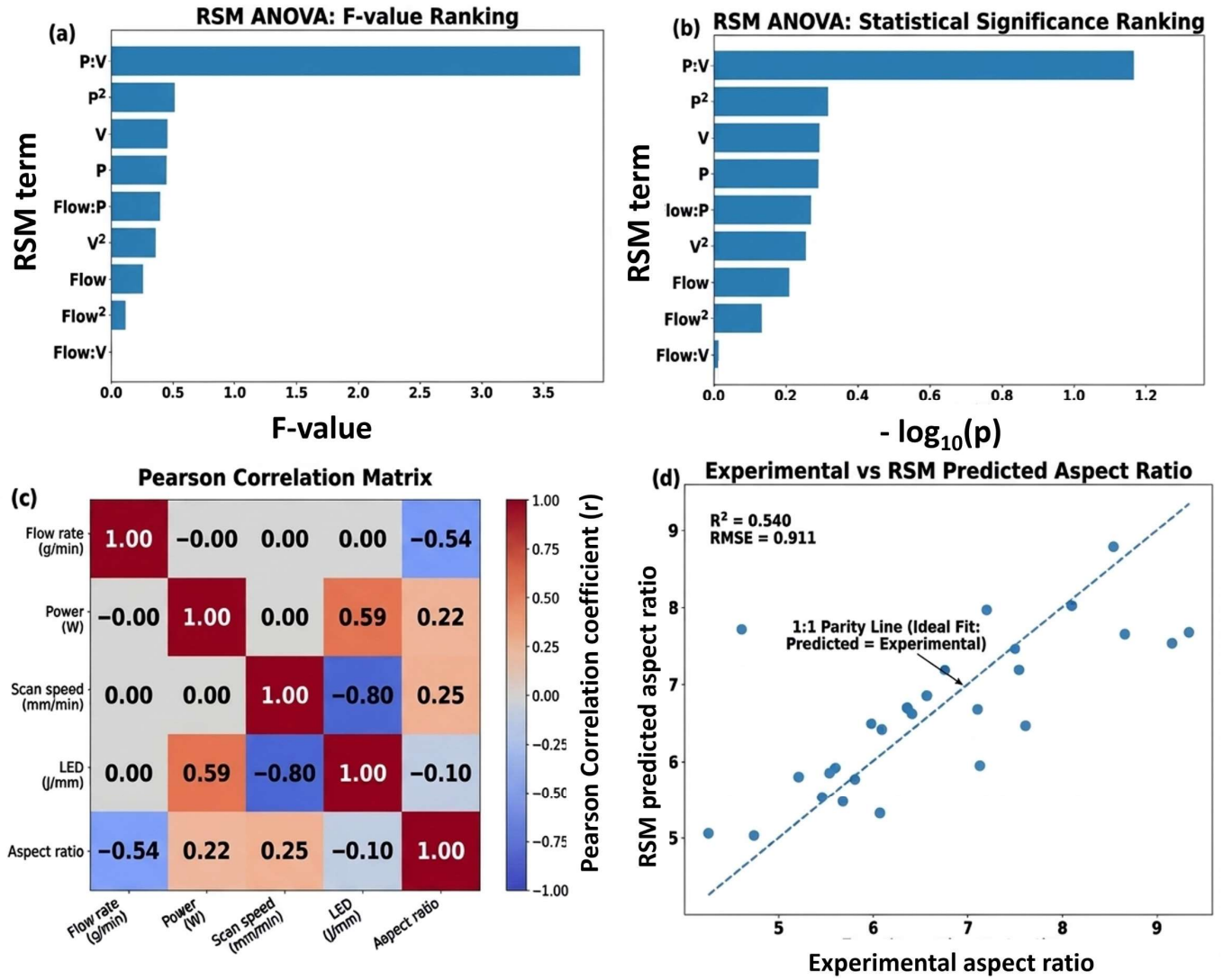

Figure 4. Statistical and correlation analysis of the single-track deposition aspect ratios, detailing (**a**) the F-value ranking of the RSM ANOVA terms, (**b**) the statistical significance ranking of the terms relative to the $p = 0.05$ threshold, (**c**) the Pearson correlation matrix for the process parameters, LED, and aspect ratio, and (**d**) the comparison between the experimental and RSM-predicted aspect ratios ($R^2 = 0.540$).

Table 2. LDED processing parameters investigated and selected for bulk deposition.

Parameter	Investigated Range	Selected Condition
Laser power (W)	700–900	900
Scanning speed (mm/min)	500–700	600
Powder feed rate (g/min)	2.8–4.0	3.4
Number of single-track parameter combinations	27	1
Track width (mm)	Varied with parameters	~2.502
Track height (mm)	Varied with parameters	~0.332
Aspect ratio (*W*/*H*)	Varied with parameters	~7.54

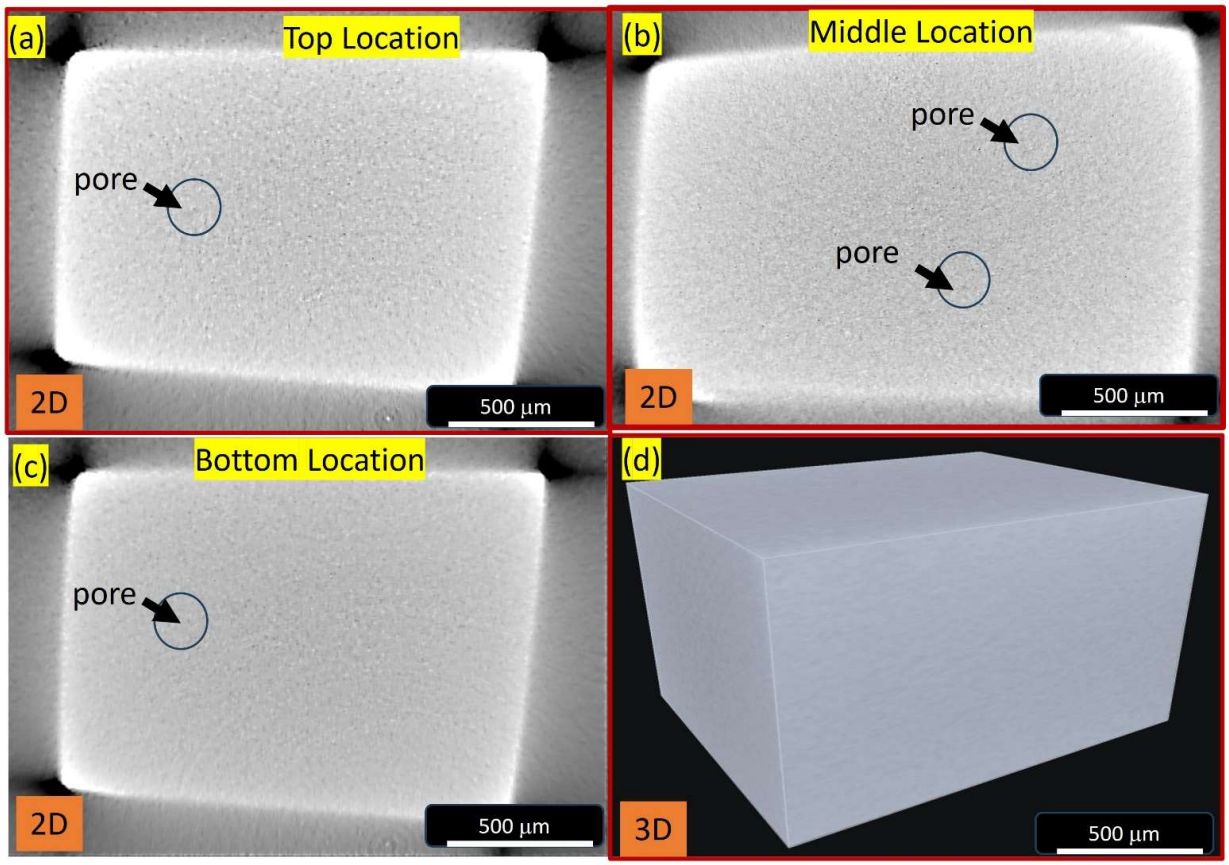

Figure 5. (**a**–**d**) Micro-CT evaluation of Ti-6Al-4V bulk deposit (900 W, 600 mm/min, 3.4 g/min) showing representative 2D slices from (**a**) top, (**b**) middle, and (**c**) bottom regions, and (**d**) the 3D volumetric reconstruction.

3.2. Microstructure and Phase Stability of LDED-Built Ti-6Al-4V

Optical micrographs of the LDED-built Ti-6Al-4V alloy obtained at different magnifications are presented in Figure 6a–d. Figure 6a provides an overview of the substrate, heat-affected zone (HAZ), and deposited region, while the corresponding higher-magnification micrographs are presented in Figure 6b–d. The substrate and HAZ exhibit a typical basket-weave/Widmanstätten morphology consisting of α laths separated by thin β regions within the prior-β grain structure. The prior-β grain boundaries are relatively well delineated and exhibit a comparatively polygonal morphology. Such a transformed $\alpha + \beta$ morphology is characteristic of Ti-6Al-4V subjected to thermally driven $\beta \rightarrow \alpha$ transformation during cooling. The morphology and scale of the transformed α phase strongly depend on the cooling rate and subsequent thermal cycles experienced during processing. In contrast, the deposited region exhibits distinctly elongated prior-β grains that preferentially extend along the build direction, as evident in Figure 6b. The development of such columnar prior-β grains is characteristic of LDED built Ti-6Al-4V and is generally associated with directional solidification and epitaxial growth from the underlying material.

During deposition, the substrate and previously deposited layers act as nucleation sites, while the steep temperature gradient and the direction of heat extraction favor the growth of β grains along the direction opposite to the dominant heat-flow direction. Consequently, previously formed β grains can survive across successive deposition layers and grow epitaxially, producing elongated columnar prior-β grains aligned approximately parallel to the build direction. Similar columnar prior-β morphologies have been widely reported for LDED-built Ti-6Al-4V [15,16].

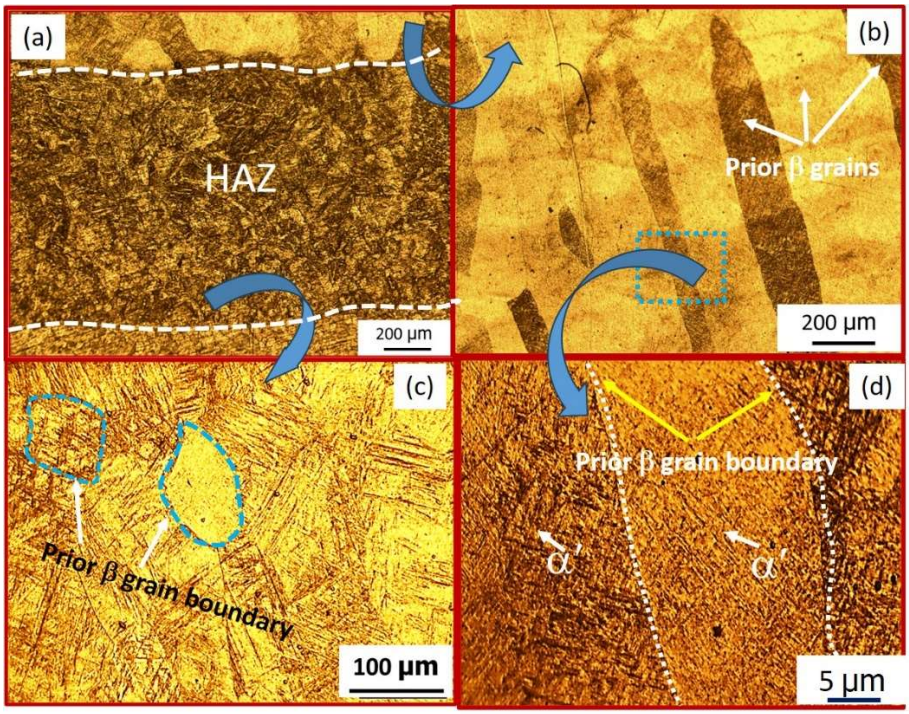

Figure 6. Optical micrographs of the LDED Ti-6Al-4V deposit showing different regions and characteristic microstructural constituents: (**a**) heat-affected zone (HAZ) delineated by dashed lines; (**b**) elongated columnar prior-*β* grains in the deposited region; (**c**) prior-*β* grain morphology and corresponding grain boundaries at higher magnification; and (**d**) α and α′ phases within the prior-*β* grains, highlighting the microstructural features near the prior-*β* grain boundaries.

The higher-magnification micrographs in Figure 6c,d further reveal a fine acicular/lamellar transformation product within the prior-*β* grains. The pronounced refinement of these features relative to the substrate and HAZ can be attributed to the rapid and highly non-equilibrium thermal cycles associated with laser deposition. Depending on the local cooling rate and reheating history, the high-temperature *β* phase in Ti-6Al-4V can transform either through diffusional $\beta \rightarrow \alpha + \beta$ transformation or, at sufficiently high cooling rates, through a diffusionless $\beta \rightarrow \alpha'$ martensitic transformation. Therefore, the fine acicular morphology observed in the deposited region suggests the presence of a substantial metastable transformation product; however, optical microscopy alone is insufficient to distinguish unambiguously between *α* and α'.

The SEM micrographs presented in Figure 7a–c provide further insight into the hierarchical morphology of the deposited material. Prominent acicular plates are observed within the prior-*β* grains, together with finer secondary laths and inter-lath regions. The morphology is consistent with a predominantly martensitic/transformed microstructure expected from the relatively high cooling rates associated with the LDED process. Previous investigations have reported that LDED Built Ti-6Al-4V can contain combinations of acicular α', fine *α* laths, retained *β*, and other transformation products depending on the local thermal history and cooling rate [16]. At higher magnification, Figure 7c additionally reveals a series of closely spaced, parallel contrast features within selected acicular plates. These features suggest internal twinning or twin-like substructures within the martensitic plates; their crystallographic identity as nano-twins was definitively confirmed through subsequent high-resolution EBSD analysis (Figure 8). The inverse pole figure (IPF) shown in Figure 8a reveals that the formation of such deformation/twinning substructures can be associated with the high supersaturation and lattice strain of the metastable α' martensite generated during rapid $\beta \rightarrow \alpha'$ transformation. The α' phase forms through a diffusionless transformation and can retain a composition close to that of the parent *β* phase [24]. Under these non-equilibrium conditions, the high internal strain and limited number of readily activated slip systems may

promote alternative accommodation mechanisms, including twinning. In addition, the phase analysis shown in Figure 8b further elucidates the microstructural composition. The corresponding phase map demonstrates that the deposit is predominantly composed of the $\frac{\alpha}{\alpha'}$ phase, which accounts for 93.5% of the analyzed area. The retained β phase accounts for the remaining 6.5% of the phase fraction and exhibits two distinct morphologies: lamellar structures distributed between the α laths and isolated globular β particles.

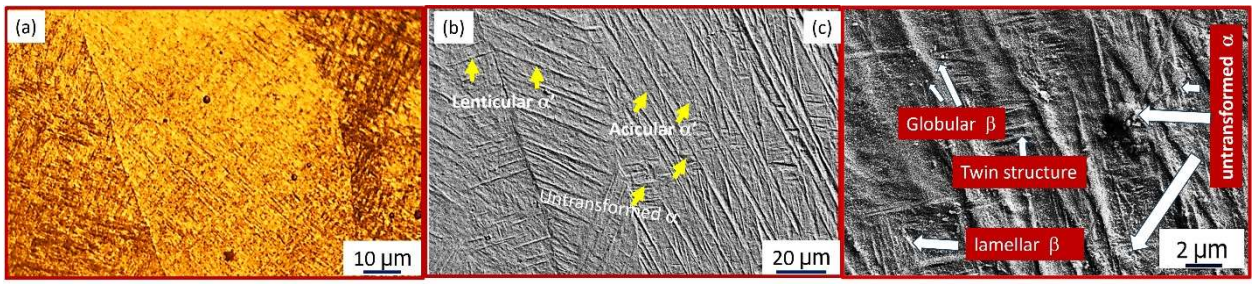

Figure 7. Microstructural features of the LDED Ti-6Al-4V deposit at different magnifications: (**a**) optical micrograph showing the morphology of the deposited microstructure; (**b**) SEM micrograph highlighting lenticular α, acicular α' and untransformed α features; and (**c**) higher-magnification SEM micrograph illustrating globular β, lamellar β, twin structures and untransformed α.

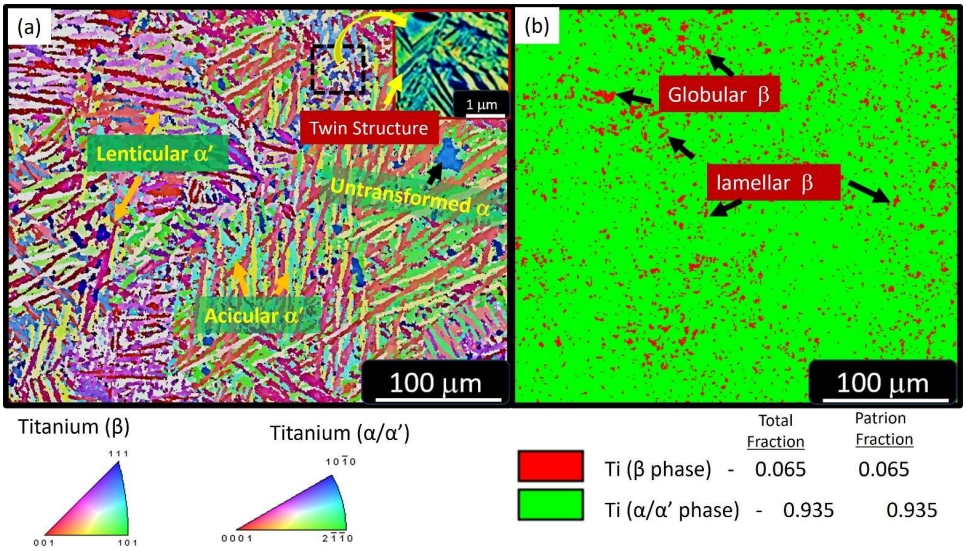

Figure 8. EBSD analysis of the LDED built Ti-6Al-4V. (**a**) Inverse pole figure (IPF) map highlighting lenticular α', acicular α', and untransformed α, with a high-magnification inset showing twin formation. (**b**) Phase map displaying the dominant α/α' phase (green, 93.5%) alongside retained β phase (red, 6.5%) in both globular and lamellar morphologies.

To further investigate the chemical partitioning associated with the observed microstructural constituents, quantitative point EDS analysis was performed on selected microstructural features, and the corresponding elemental compositions are presented in Figure 9. The analysis confirms distinct elemental segregation: the regions marked as Figure 9b,d exhibit relatively higher Al concentrations (6.3–6.7 wt%) and lower V concentrations (3.8–4.1 wt%), whereas regions Figure 9a,c show comparatively higher V concentrations (6.2–6.8 wt%) and lower Al concentrations (4.2–4.6 wt%). This quantitative distribution is consistent with the well-established partitioning tendency of Al toward the α phase and V toward the β phase in Ti-6Al-4V. Accordingly, the EDS observations are further correlated with the diffraction results presented in Figure 10 for phase identification. High-resolution synchrotron X-ray diffraction measurements were subsequently performed at an incident photon energy of 17 keV, and the resulting diffraction pattern is presented in Figure 10. The diffraction pattern is dominated by reflections corresponding to the hexagonal α-type structure. The observed peak positions and profiles are consistent

with the presence of α/α' phases, which cannot be reliably separated solely on the basis of peak positions because α' is a supersaturated hexagonal martensitic phase with crystallographic parameters close to those of equilibrium α-Ti. The calculated lattice parameters for these phases are α (a = 0.293 nm, c = 0.467 nm) and α' (a = 0.295 nm, c = 0.468 nm) [25]. The observed peak positions and profiles are consistent with the presence of α/α' phases, which cannot be reliably separated solely on the basis of peak positions because α' is a supersaturated hexagonal martensitic phase with crystallographic parameters close to those of equilibrium α-Ti. In addition to the dominant α/α' reflections, weak reflections attributable to the body-centered cubic β phase (a = 0.2263 nm) are observed at higher diffraction angles. The criteria for identifying these weak peaks relied on matching secondary low-intensity signals distinct from the primary HCP reflections. The presence of these weak β reflections indicate that a limited fraction of β is retained after cooling, which is consistent with the V enriched regions identified by EDS. Furthermore, phase fraction quantification via EBSD phase mapping (Figure 8) confirmed a constitution of 93.5% α/α' and 6.5% retained β. Very weak features that may be associated with an orthorhombic α'' martensitic structure (a = 0.3135 nm, b = 0.4763 nm, c = 0.4576 nm) are also observed in the diffraction pattern. However, because α'' reflections overlap significantly with the much stronger α/α' reflections, their identification from weak overlapping peaks alone should be treated cautiously. The coexistence of α/α' and retained β is commonly reported in rapidly processed Ti-6Al-4V alloys and reflects the incomplete transformation of the high-temperature β phase during the non-equilibrium cooling cycle. Therefore, the present XRD results provide evidence that the microstructure is predominantly composed of α/α'-type phases with a limited fraction of retained β and minor α'' phases. Similar coexistence of α' and small amounts of α'' has been reported in additively manufactured Ti-6Al-4V [17,22], although the relative fractions are strongly dependent on processing conditions and thermal history. The development of this fine acicular/needle-like morphology is driven by the specific mechanism of martensitic transformation under extreme thermal gradients. During the LDED process, the material is heated well above the β-transus temperature. The subsequent rapid heat extraction to the substrate and surrounding atmosphere results in cooling rates that easily exceed the critical threshold required to suppress diffusion-controlled phase transformations. Consequently, the high-temperature body-centred cubic (BCC) β phase undergoes a diffusionless, displacive (shear) transformation to the metastable hexagonal close-packed (HCP) α' martensite. Because no atomic diffusion or elemental partitioning (of Al and V) can occur at these cooling rates, the transforming region undergoes a cooperative, short-range movement of atoms. This displacive mechanism generates substantial internal lattice strain. To accommodate this strain, the α' phase develops into highly refined, acicular (needle-like) plates characterized by a high density of crystalline defects, including the nano-twins observed in the EBSD and SEM analyses. Overall, the combined OM, SEM, EDS, and synchrotron XRD results indicate that the LDED built Ti-6Al-4V possesses a hierarchical non-equilibrium microstructure consisting predominantly of elongated prior-β grains containing fine acicular α/α' transformation products, together with a small fraction of retained β and possibly a minor α'' constituent. The formation of elongated prior-β grains is associated primarily with directional solidification and epitaxial growth, whereas the refinement and martensitic character of the intragranular transformation products are governed by the rapid thermal cycling and cooling experienced during LDED. The compositional partitioning observed by EDS, particularly Al enrichment in α-enriched regions and V enrichment in β-enriched regions, is consistent with the expected phase chemistry and further supports the phase constitution derived from the diffraction analysis. While the combination of processing history, acicular morphology, and EBSD-confirmed nano-twinning strongly suggests a predominantly martensitic (α') structure, it must be noted that standard EBSD and synchrotron XRD cannot definitively separate the structurally similar α and α' phases, nor unambiguously confirm the trace presence of the orthorhombic α'' phase [22]. The absolute crystallographic separation of the α and α' variants, as well as the definitive verification of the α'' phase fraction, requires nanoscale characterisation via Transmission Electron Microscopy (TEM), which remains a subject for necessary future investigations.

While the current experimental observations, such as the formation of metastable α' martensite and the highly refined acicular morphology, qualitatively confirm the presence of the extreme thermal gradients and rapid cooling rates inherent to the LDED process, this phenomenological study does not currently include quantitative numerical simulations of the thermal history. Fully quantifying the complex thermal cycles, including the spatial temperature distribution and localized cooling rates, requires advanced finite-element modelling (FEM). Such numerical simulations will form the basis of future investigations to mathematically bridge the gap between specific energy input parameters, localized thermal histories, and the resulting thermodynamic phase fractions.

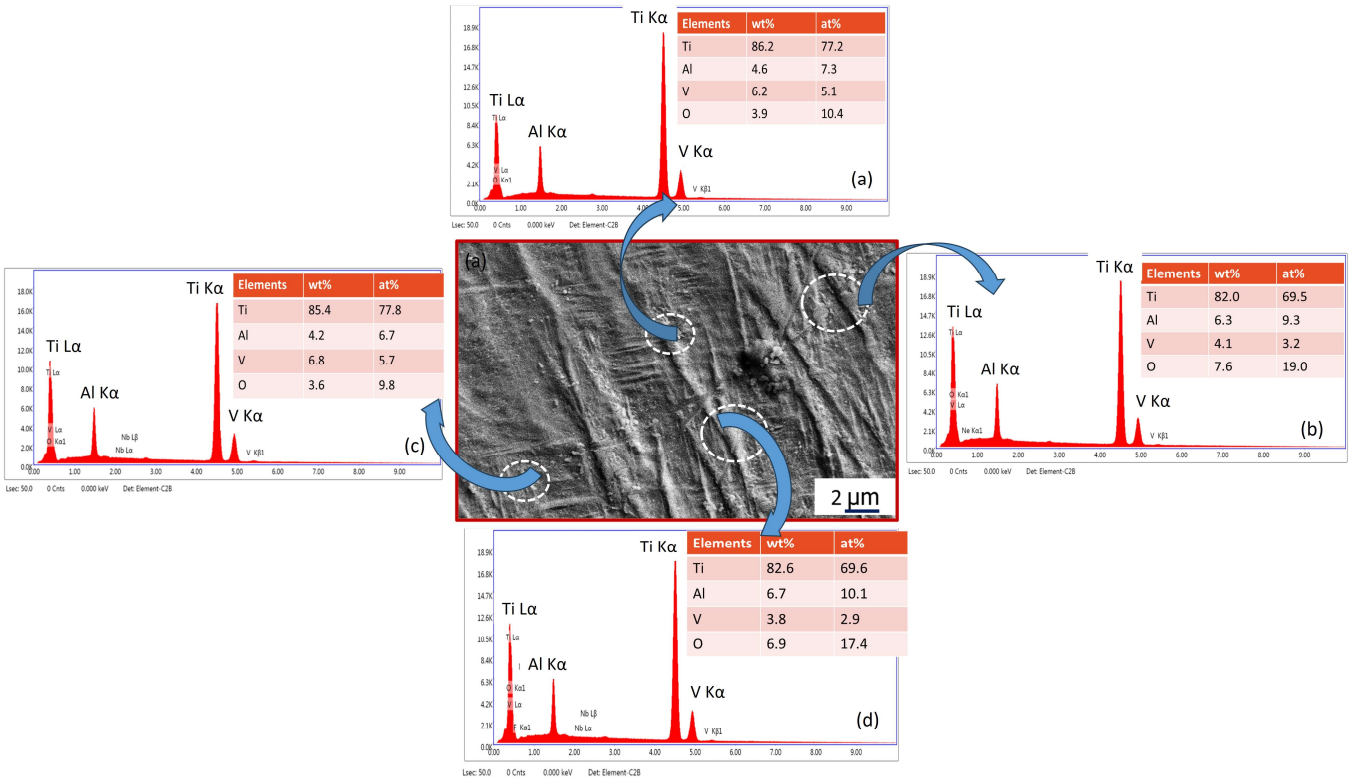

Figure 9. SEM micrograph of LDED built Ti-6Al-4V (center) and (**a**–**d**) corresponding point EDS analysis of marked locations showing the formation of α and β rich region, (**b**,**d**) regions correspond to α rich phase and (**a**,**c**) region correspond to β rich phase.

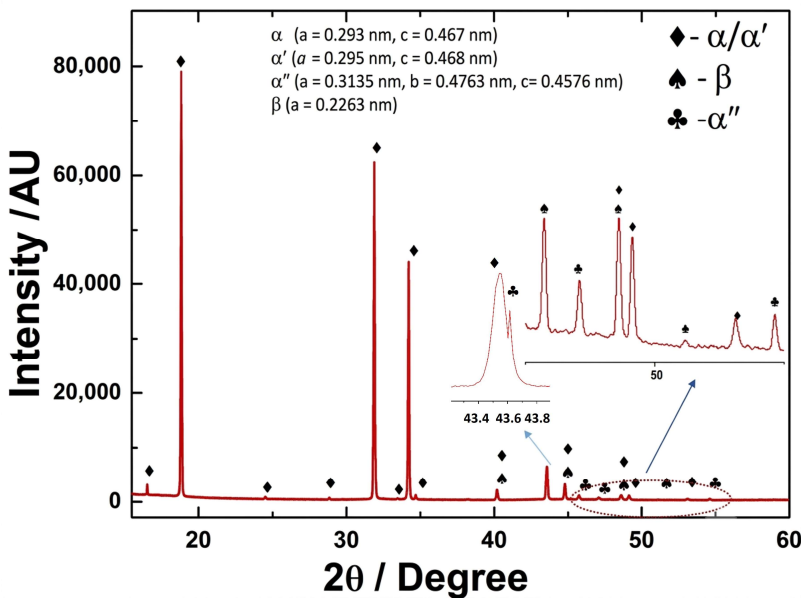

Figure 10. Synchrotron XRD pattern of LDED-built Ti-6Al-4V.

3.3. Microhardness and Tensile Property Evaluation

The Vickers microhardness distribution across the substrate, heat-affected zone (HAZ), and deposited region of the LDED built Ti-6Al-4V specimen is presented in Figure 11. A continuous line scan was conducted along the build direction, applying a load of 0.1 kgf with a dwell time of 10 s for all indents. A clear increase in microhardness is observed from the substrate toward the deposited region, indicating the significant influence of the LDED thermal cycle on the microstructural state of the material. The substrate exhibits a relatively uniform microhardness in the range of 174–176 $HV^{0.1}$, representing the microhardness of the initial base material. In the HAZ, the microhardness increases progressively to approximately 187–241 $HV^{0.1}$. This variation can be attributed primarily to the localized thermal cycles imposed by the moving laser heat source and modification in composition due to dilution effect. During LDED, the material adjacent to the melt pool undergoes rapid heating and subsequent cooling, which alters the morphology, phase stability, and distribution of the α and β phases. The resulting microstructural modification within the HAZ leads to a gradual change in microhardness compared with the unaffected substrate. Similar microhardness variations across the substrate and HAZ region have been reported in laser-based processing of Ti-6Al-4V and have been associated with local thermal histories and phase transformations [21,25]. A substantial increase in microhardness is observed in the deposited region, where the measured values range from approximately 377 to 434 $HV^{0.1}$. The variation in microhardness across different regions is tabulated in Table 3, with possible justifications. This pronounced enhancement is associated with the refined non-equilibrium microstructure generated under the rapid thermal cycling of the LDED process. While this hardness increase is driven by a combination of microstructural factors, their relative contributions to macroscopic strength vary. The dominant strengthening mechanisms are grain boundary strengthening (the Hall-Petch effect) and dislocation strengthening. The extreme geometric refinement of the metastable α' martensite laths provides a highly dense network of inter-lath boundaries that effectively impede dislocation motion during deformation. Concurrently, the displacive, diffusionless $\beta \rightarrow \alpha'$ transformation generates substantial internal lattice strain and a massive inherent density of crystallographic defects that strictly resist plastic deformation [19,22]. In contrast, twinning deformation and solid-solution supersaturation act as secondary strengthening contributors. Although the nano-twins (as confirmed by the EBSD analysis) serve as robust, localized barriers to dislocation glide, their limited overall volume fraction restricts their global influence on macroscopic microhardness compared to the pervasive lath boundaries. Furthermore, a notable spatial fluctuation in microhardness is observed within the deposited region itself, with values ranging from 377 to 434 $HV^{0.1}$. This variation is directly governed by the complex interlayer thermal cycling inherent to the layer-by-layer LDED process. During the deposition of successive layers, previously solidified material undergoes repeated reheating. This cyclic thermal exposure acts as an *in-situ* tempering process. Depending on the peak temperature attained during reheating, the highly strained, metastable α' martensite in the underlying layers undergoes partial tempering and decomposition, resulting in a finer mixture of equilibrium α and β phases. This decomposition process relieves internal lattice strain and locally increases the volume fraction of the softer retained β phase, leading to periodic localized softening within the build volume. Conversely, the uppermost layers, which experience the most rapid final cooling and are not subjected to subsequent reheating, retain a higher fraction of untempered, highly strained α' martensite, generally corresponding to the upper bound of the measured microhardness range. Therefore, the spatial fluctuations in the microhardness profile serve as a mechanical footprint of the varying degrees of α' tempering, lattice strain relaxation, and retained β distribution induced by the localized thermal history of the multilayer build [19,21]. A limitation of the present characterisation is the inability to precisely mathematically decouple these overlapping contributions. Quantifying the exact contributions of lath spacing, dislocation density, and twinning to the measured microhardness would require dedicated characterization techniques, such as nanoindentation and high-resolution X-ray diffraction (XRD) peak-

broadening analysis. Nevertheless, the observed microhardness range of 377–434 $HV^{0.1}$ is highly consistent with values reported for rapidly solidified or martensitic Ti-6Al-4V produced using laser-based additive manufacturing processes [16,17].

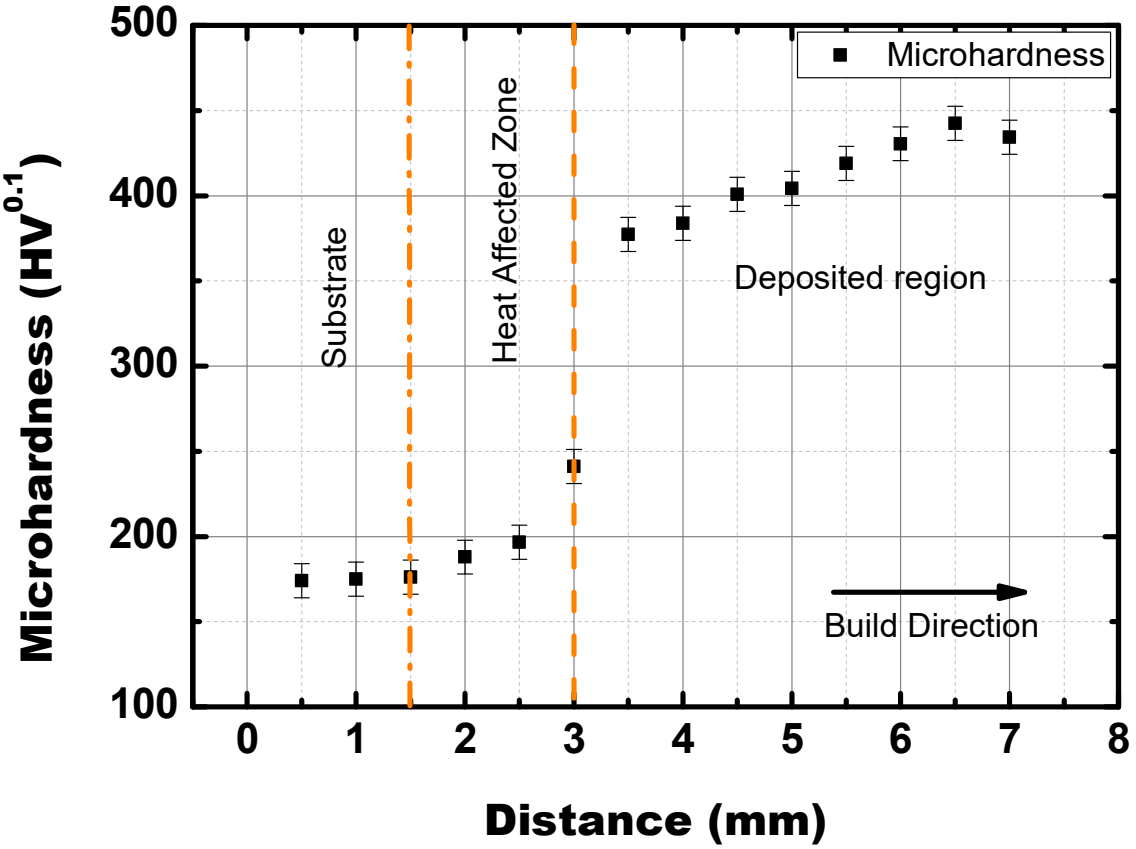

Figure 11. Microhardness variation of LDED-built Ti-6Al-4V across the substrate, heat affected zone and deposited region.

Table 3. Microhardness variation across the substrate, HAZ and deposit regions.

Region of Interest	Microhardness ($HV^{0.1}$)	Interpretation
Substrate	174–176	Comparatively lower microhardness
Heat-affected zone (HAZ)	187–241	Intermediate microhardness, reflecting the local thermal history
Deposited region	377–434	Higher microhardness associated with the refined α/α′-dominated microstructure

To assess the macroscopic mechanical anisotropy associated with the highly directional columnar prior-β grain structure, tensile testing was conducted at room temperature. Figure 12 presents the engineering stress versus total elongation curves for specimens loaded along three primary axes: the build direction, the scan direction, and the orthogonal direction. The LDED deposited Ti-6Al-4V exhibits exceptional overall mechanical performance across all tested orientations. The measured ultimate tensile strength and total elongation were similar across the three tested orientations, with UTS values of approximately 980–1000 MPa and elongation values of 18–18.5%. Differences were observed in the yielding and early strain-hardening portions of the stress–strain curves, suggesting orientation-dependent deformation behavior. However, additional replicate testing and statistical analysis are required to establish the significance of these differences and to determine the extent of tensile anisotropy [4]. The specimen loaded along the build direction exhibits a notably lower initial stress response and strain hardening rate compared to the scan and orthogonal directions. This mechanical variance is a direct consequence of the macrostructural morphology. When loaded parallel to the build direction, the tensile axis aligns with the

long axis of the columnar prior-β grain boundaries. Because these extended boundaries present fewer transverse barriers to initial dislocation glide compared to orthogonal loading, macroscopic yielding and plastic flow initiate at lower applied stresses. Nevertheless, the convergence of the UTS (~980–1000 MPa) and elongation values (~18–18.5%) demonstrates that the refined α' martensitic substructure ensures robust, high-strength load-bearing capabilities irrespective of the primary columnar grain orientation [2,3].

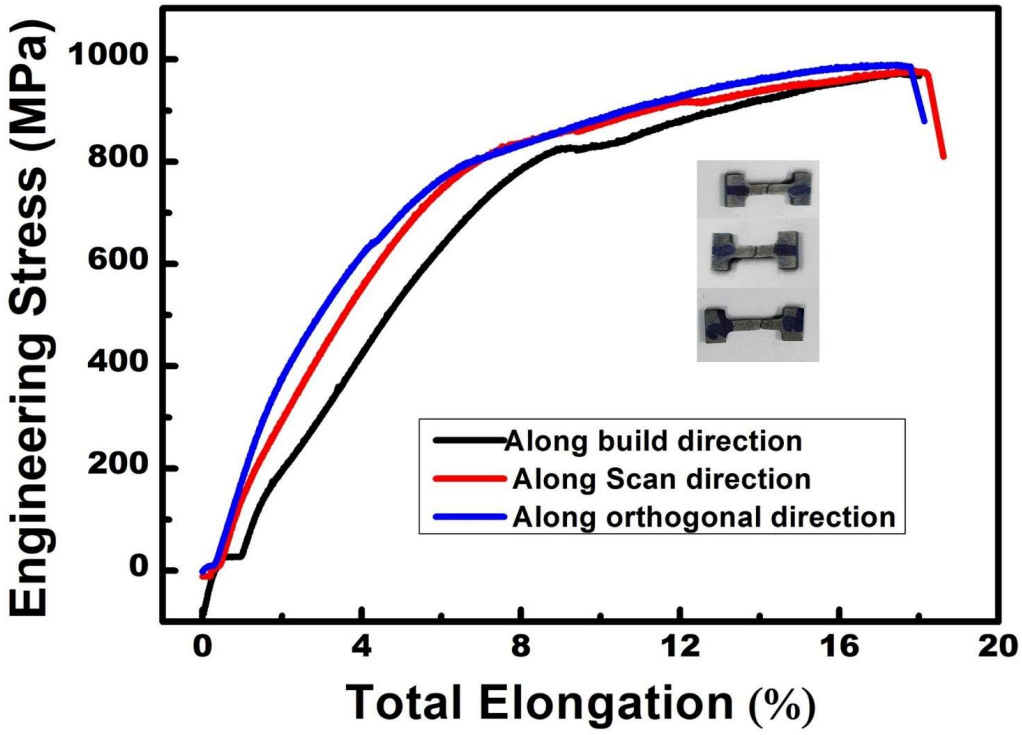

Figure 12. Engineering Stress-Strain Curve of LDED built Ti-6Al-4V.

4. Conclusions

Based on the systematic process optimization, micro-CT defect characterization, and high-resolution microstructural and mechanical analyses of the LDED-built Ti-6Al-4V alloy, the following conclusions are drawn:

I. A robust processing window for structural deposition was established at a laser power of 900 W, scanning speed of 600 mm/min, and powder feed rate of 3.4 g/min. Statistical analysis confirmed that linear energy density (LED) alone is an insufficient predictor of track aspect ratio (W/H) due to non-linear parameter interactions, necessitating combined geometric and morphological evaluation.

II. Bulk components printed under the optimized condition achieved a near-theoretical density of 99.54% (porosity < 0.5%). 3D micro-CT reconstructions verified that the defects were limited to a small number of isolated, spherical gas pores, with no evidence of interconnected void networks, lack-of-fusion regions, or macroscopic cracking.

III. The deposit exhibits distinctly elongated prior-β grains aligned parallel to the build direction, driven by steep thermal gradients and epitaxial growth from the substrate. High cooling rates suppress diffusion, generating a hierarchical matrix dominated by 93.5% metastable α′ martensite populated with crystalline nano-twins to accommodate transformation strain, alongside 6.5% retained β phase in globular and lamellar morphologies.

IV. A strong microhardness gradient was recorded across the zones, increasing from 174–176 $HV^{0.1}$ in the substrate to 187–241 $HV^{0.1}$ in the HAZ, and peaking at 377–434 $HV^{0.1}$ in the deposit. Periodic microhardness fluctuations within the deposited region serve as a mechanical footprint of cyclic, layer-

by-layer reheating, potentially associated with repeated tempering, strain relaxation, and variations in the α/α' microstructure, including possible α'' phase formation.

V. The deposit demonstrates excellent tensile properties across all primary testing directions, maintaining a high ultimate tensile strength of 980–1000 MPa and an exceptional total elongation of 18–18.5%. While final strength and ductility remain isotropic, the orientation of the columnar prior-β boundaries causes distinct yielding and early strain-hardening anisotropy when tensile loads are applied parallel to the build direction.

Acknowledgments

The authors sincerely acknowledge Anil Adbol, Lalit, Sokhen Tudu, Dinesh Kumar Singh, and Suresh Kumar for their valuable technical assistance and support during the experimental work. The authors also acknowledge the members of the Additive Manufacturing Technology Laboratory, RRCAT, for their cooperation, technical interactions, and constructive discussions throughout the course of this research. Their assistance in facilitating the experimental activities and characterisation work is gratefully acknowledged.

Author Contributions

Conceptualization, Methodology, Data collection A.P. and P.P.; Analysis, Writing-Original Draft Preparation by A.P.; Writing-Review & Editing done by A.K.R.; Investigation, Visualization, and Supervision done by A.K.R. and C.P.P.

Ethics Statement

Not Applicable.

Informed Consent Statement

Not Applicable.

Data Availability Statement

Data used in this research are available upon reasonable request.

Funding

This research received no external funding.

Declaration of Competing Interest

No conflict of interest.

References

1. Davim JP. (Ed.). *Lasers in Manufacturing*; John Wiley & Sons: Hoboken, NJ, USA, 2012. DOI:10.1002/9781118562857
2. Liu S, Shin YC. Additive manufacturing of Ti6Al4V alloy: A review. *Mater. Des.* **2019**, *164*, 107552. DOI:10.1016/j.matdes.2018.107552
3. Azarniya A, Colera XG, Mirzaali MJ, Sovizi S, Bartolomeu F, St Weglowski M, et al. Additive manufacturing of Ti–6Al–4V parts through laser metal deposition (LMD): Process, microstructure, and mechanical properties. *J. Alloys Compd.* **2019**, *804*, 163–191. DOI:10.1016/j.jallcom.2019.04.255
4. Nguyen HD, Pramanik A, Basak AK, Dong Y, Prakash C, Debnath S, et al. A critical review on additive manufacturing of Ti-6Al-4V alloy: Microstructure and mechanical properties. *J. Mater. Res. Technol.* **2022**, *18*, 4641–4661. DOI:10.1016/j.jmrt.2022.04.055

5. Gonnabattula A, Thanumoorthy RS, Bontha S, Balan ASS, Kumar VA, Kanjarla AK. Process parameter optimization for laser directed energy deposition (LDED) of Ti6Al4V using single-track experiments with small laser spot size. *Opt. Laser Technol.* **2024**, *175*, 110861. DOI:10.1016/j.optlastec.2024.110861
6. Kelly SM, Kampe SL. Microstructural evolution in laser-deposited multilayer Ti-6Al-4V builds: Part I. Microstructural characterization. *Metall. Mater. Trans. A* **2004**, *35*, 1861–1867. DOI:10.1007/s11661-004-0094-8
7. Xu Y, Lu Y, Sundberg KL, Liang J, Sisson RD. Effect of Annealing Treatments on the Microstructure, Mechanical Properties and Corrosion Behavior of Direct Metal Laser Sintered Ti-6Al-4V. *J. Mater. Eng. Perform.* **2017**, *26*, 2572–2582. DOI:10.1007/s11665-017-2710-y
8. Tan H, Guo M, Clare AT, Lin X, Chen J, Huang W. Microstructure and properties of Ti-6Al-4V fabricated by low-power pulsed laser directed energy deposition. *J. Mater. Sci. Technol.* **2019**, *35*, 2027–2037. DOI:10.1016/j.jmst.2019.05.008
9. Kelly SM, Kampe SL. Microstructural evolution in laser-deposited multilayer Ti-6Al-4V builds: Part II. Thermal modeling. *Metall. Mater. Trans. A* **2004**, *35*, 1869–1879. DOI:10.1007/s11661-004-0095-7
10. Ahmed T, Rack HJ. Phase transformations during cooling in α + *β* titanium alloys. *Mater. Sci. Eng. A* **1998**, *243*, 206–211. DOI:10.1016/S0921-5093(97)00802-2
11. Thijs L, Verhaeghe F, Craeghs T, Van Humbeeck J, Kruth JP. A study of the microstructural evolution during selective laser melting of Ti–6Al–4V. *Acta Mater.* **2010**, *58*, 3303–3312. DOI:10.1016/j.actamat.2010.02.004
12. Muiruri A, Maringa M, du Preez W. Crystallographic Texture Analysis of As-Built and Heat-Treated Ti6Al4V (ELI) Produced by Direct Metal Laser Sintering. *Crystals* **2020**, *10*, 699. DOI:10.3390/cryst10080699
13. Mishra GK, Rai AK, Gupta P, Karthik V, Paul CP. Studies on Microstructural Stability, Thermomechanical Properties, and Electrochemical Behavior of LDED-built SS 316LN Steel. *J. Mater. Eng. Perform.* **2026**, *35*, 26945–26962. DOI:10.1007/s11665-026-13603-w
14. Yadav S, Rai AK, Kausal SS, Paul CP. A novel coupled model for microstructural evolution prediction during laser additive manufacturing: Data driven and physics driven modelling. *Prog. Addit. Manuf.* **2025**, *10*, 6109–6118. DOI:10.1007/s40964-025-00955-3
15. Nourollahi A, Shoja Razavi R, Barekat M, Vakilzadeh Anaraki M, Erfanmanesh M. Microstructural investigation of direct laser deposition of the Ti–6Al–4V alloy by different melt pool protection conditions. *J. Mater. Res. Technol.* **2021**, *13*, 590–601. DOI:10.1016/j.jmrt.2021.04.087
16. Davim JP. Titanium alloys: A bibliometric analysis. *Int. J. Mater. Eng. Innov.* **2025**, *16*, 273–275. Available online: https://www.inderscience.com/info/dl.php?filename=2025/ijmatei-8738.pdf (accessed on 10 October 2026).
17. Davim JP, Oliveira C, Cardoso A. Predicting the geometric form of clad in laser cladding by powder using multiple regression analysis (MRA). *Mater. Des.* **2008**, *29*, 554–557. DOI:10.1016/j.matdes.2007.01.023
18. Hama-Saleh R, Yildirim K, Hemes S, Weisheit A, Häfner CL. Investigation of High-Deposition-Rate Additive Manufacturing of Ti-6Al-4V via Laser Material Deposition. In Proceedings of the 24th International ESAFORM Conference on Material Forming (ESAFORM 2021), Online, 14–16 April 2021. DOI:10.25518/esaform21.486
19. Zhang J, Cao Y, Wang H, Shi T, Su B, Zhang L. Effect of Annular Laser Metal Deposition (ALMD) Process Parameters on Track Geometry and Thermal History on Ti6Al4V Alloy Clad. *Materials* **2023**, *16*, 4062. DOI:10.3390/ma16114062
20. Rai AK, Paul CP, Mishra GK, Singh R, Rai SK, Bindra KS. Study of microstructure and wear properties of laser borided Inconel 718. *J. Mater. Process. Technol.* **2021**, *298*, 117298. DOI:10.1016/j.jmatprotec.2021.117298
21. Saboori A, Tusacciu S, Busatto M, Lai M, Biamino S, Fino P, et al. Production of Single Tracks of Ti-6Al-4V by Directed Energy Deposition to Determine the Layer Thickness for Multilayer Deposition. *J. Vis. Exp.* **2018**, *133*, e56966. DOI:10.3791/56966
22. Kazantseva N, Krakhmalev P, Thuvander M, Yadroitsev I, Vinogradova N, Ezhov I. Martensitic transformations in Ti-6Al-4V (ELI) alloy manufactured by 3D Printing. *Mater. Charact.* **2018**, *146*, 101–112. DOI:10.1016/j.matchar.2018.09.042
23. Ávila Calderón LA, Graf B, Rehmer B, Petrat T, Skrotzki B, Rethmeier M. Characterisation of Ti–6Al–4V Fabricated by Multilayer Laser Powder-Based Directed Energy Deposition. *Adv. Eng. Mater.* **2022**, *24*, 2101333. DOI:10.1002/adem.202101333
24. Zhong HZ, Zhang XY, Wang SX, Gu JF. Examination of the twinning activity in additively manufactured Ti-6Al-4V. *Mater. Des.* **2018**, *144*, 14–24. DOI:10.1016/j.matdes.2018.02.015
25. Mahamood RM, Akinlabi ET. Scanning Speed Influence on the Microstructure and Micro hardness Properties of Titanium Alloy Produced by Laser Metal Deposition Process. *Mater. Today Proc.* **2017**, *4*, 5206–5214. DOI:10.1016/j.matpr.2017.05.028